

Article

Origin of Qinxì Silver Polymetallic Deposit in Southeast Coast, China: Evidences from H–O–S–Pb Isotopes and Mineral Rb–Sr Geochronology

Senfang Zhong^{1,2}, Wenhao Liu^{1,*}, Jun Zhang¹ and Qiuling Gan²

¹ Faculty of Earth Resources, China University of Geosciences, Wuhan 430074, China; zsf2836635@163.com (S.Z.); zhangjun@cug.edu.cn (J.Z.)

² Fourth Geological Brigade of Fujian Province, Ningde 352100, China; 15120191155041@stu.xmu.edu.cn

* Correspondence: liuwh@cug.edu.cn

Abstract: The Qinxì silver deposit is located in eastern Fujian Province, South China. It is hosted in the late Jurassic Nanyuan volcanic unit and controlled spatially by structural alteration zone. The origins of the deposit are understood poorly. In this study, systematic field geology, precise sulfide geochronology, and H–O–S–Pb isotope analyses were carried out. The symbiotic minerals and ore assemblages are interpreted as evidence that Qinxì ore is a typical middle to low temperature hydrothermal deposit. Galena and sphalerite from the ore yield a Rb–Sr isochronal age of 130 ± 2.0 Ma (MSWD = 1.7), and single galena samples yield a Rb–Sr isochronal age of 130 ± 7.1 Ma (MSWD = 2) and are evidence that the ore was formed in the early Cretaceous period. The silver-bearing quartz vein has O:H and $^{18}\text{O}:^{16}\text{O}$ ratios intermediately between magmatic and meteoric water ($\delta^{18}\text{O}_{\text{water-smow}}$ from -2.50‰ to -0.1‰ and $\delta\text{D}_{\text{v-smow}}$ from -73.6‰ to -60.7‰). The $\delta_{34}\text{S}$ values of metal sulfide are close to the primitive mantle sulfur values ($\delta_{34}\text{S} = -1.7$ to 7.1‰ , avg. = 0.92‰). The Pb isotopic compositions from the ore are similar to those of the hosted volcanic unit, with a value between the upper crust and mantle isotope composition ($^{206}\text{Pb}/^{204}\text{Pb} = 18.421\text{--}18.605$, $^{207}\text{Pb}/^{204}\text{Pb} = 15.580\text{--}15.772$, $^{208}\text{Pb}/^{204}\text{Pb} = 38.591\text{--}39.183$). Lead–zinc sulfides have mature crustal-derived Sr isotopic features ($(^{87}\text{Sr}/^{86}\text{Sr})_i = 0.7103$). Thus, the metallogenic source materials mainly came from the crust. Moreover, regional geological studies suggest that the Qinxì ore deposit was likely formed in an extensional terrane.

Keywords: sulphide Rb–Sr dating; H–O–S–Pb isotopes; Qinxì silver deposit; South China



check for updates

Citation: Zhong, S.; Liu, W.; Zhang, J.; Gan, Q. Origin of Qinxì Silver Polymetallic Deposit in Southeast Coast, China: Evidences from H–O–S–Pb Isotopes and Mineral Rb–Sr Geochronology. *Minerals* **2021**, *11*, 45. <https://doi.org/10.3390/min11010045>

Received: 23 November 2020

Accepted: 28 December 2020

Published: 31 December 2020

Publisher's Note: MDPI stays neutral with regard to jurisdictional claims in published maps and institutional affiliations.



Copyright: © 2020 by the authors. Licensee MDPI, Basel, Switzerland. This article is an open access article distributed under the terms and conditions of the Creative Commons Attribution (CC BY) license (<https://creativecommons.org/licenses/by/4.0/>).

1. Introduction

The volcanic fault-depression belt in Eastern Fujian Province is one of the most important prospective areas for silver polymetallic mineralization [1]. The main types of silver-polymetallic deposits in the belt are the hydrothermal vein type, the volcanic-subvolcanic hydrothermal type, the magmatic hydrothermal type, and the contact metasomatic type [2–4]. Since the 1980s, more than ten deposits have been discovered in this area, including the Zherong Yingshan large-size silver deposit, the Zhouning Tongcha silver deposit, the Zherong Makeng silver-polymetallic deposit, and the Pingnan Luocuo silver-lead-zinc deposit [5,6]. Previous studies focused mainly on the Zijinshan porphyry-epithermal Cu–Au metallogenic system and some large epithermal and porphyry deposits [7–9]. However, the origins of the silver-polymetallic deposits in the belt are poorly understood.

The Qinxì silver-polymetallic deposit features large-sized silver polymetallic deposits in the volcanic belt of eastern Fujian. Previous studies focused mainly on the geological characteristics of the deposits [10,11]. The sources of the ore-forming fluids and the mineralization ages are poorly understood, however. In this study, a systematic field geological study, the Rb–Sr geochronology and H–O–S–Pb isotope composition of the Qinxì silver polymetallic deposit were examined to constrain models of ore genesis.

2. Regional Geological Background

The South China block (SCB) consists of the Cathaysia Block in the southeast and the Yangtze Block in the northwest. The inner SCB has experienced three major collisions in its history. Those collisions happened mainly during the Jinning, Caledonian, and Indo–Chinese periods [12]. The Caledonian movement uplifted the folds in the study area, and new sedimentary rocks were deposited during the late Devonian [13–15]. Since the late Triassic, the study area was influenced by the continental margin activities, triggered by the subduction of the Paleo-pacific plate [16]. The continental margin magmatism reached its climax at the transition from the Jurassic to the Cretaceous periods and laid the foundation for the present regional structural frameworks [17–19]. A metallogenic belt that contains Pb–Zn–Cu–Au–Ag–W–Sn–Nb–Ta deposits was found in this area [20,21], including the Qinxi deposit (Figure 1).

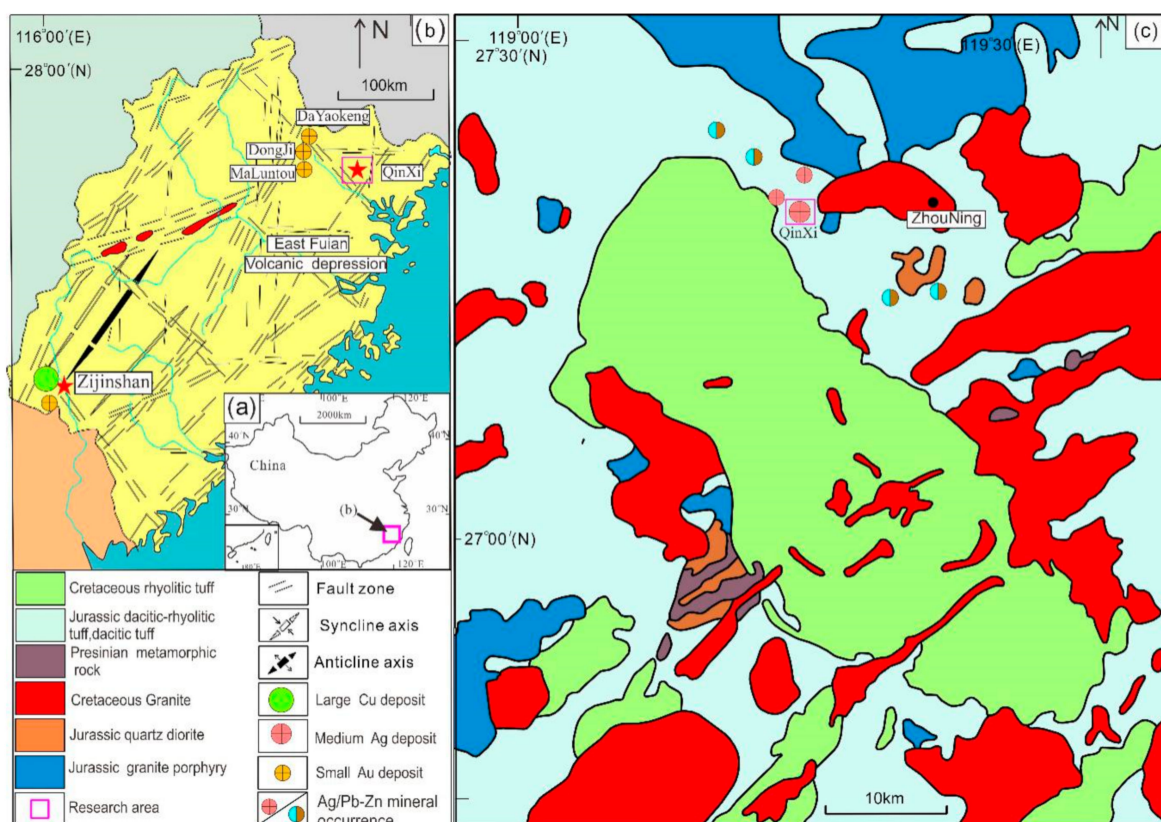


Figure 1. (a) Simplified map of China; (b) simplified geological map of Fujian Province; and (c) regional geological map of the Qinxi area (Modified from [22]).

Strata in the study area are mainly Mesozoic sedimentary–volcanic rocks, with minor Neoproterozoic metamorphic rocks and Paleozoic sedimentary rocks [22,23]. The sedimentary–volcanic rocks in the study area are divided into upper and lower volcanic rock series. Regional angular unconformities have been found between those two series of rocks. The lower volcanic rock series is composed of acid-intermediate volcanic rocks (143~115 Ma, [24]). These rocks are distributed widely in the northern Shouning, Quoting, Zhouning, and Zhenghe areas. The rock types are mainly rhyolitic ignimbrite, crystal tuff, and rhyolitic porphyroclastic lava with a maximum thickness of up to 4000 m. The upper volcanic rock series is composed of dacitic–rhyolitic volcanic rocks, with zircon U–Pb ages ranging from 113 to 85 Ma [24,25]. The upper series rocks are mainly distributed in the rift red basins of the coastal areas. Some of them are A-type volcanic rocks [26].

Besides the sedimentary–volcanic rocks, felsic intrusive rocks are also widely distributed in the study area, with the peak magmatic episodes in the Permian, late Jurassic,

early Cretaceous, and Tertiary. The late Jurassic granitoids are most widespread [27–29] among these intrusive magmatic rocks. The distributions of intrusive rocks are controlled by regional faults, which trend largely to the NNE–NE and NW.

3. Geology of the Qinxi Silver Deposit

The Qinxi mining area is located along the boundary between the early Cretaceous volcanic belt northwest of Pucheng–Ningde city and the late Jurassic volcanic belt northeast of Shouning–Meilin city (Figure 1). Outcrops in the mining area are mainly volcanic rocks from the Nanyuan Formation and Shimoshan Group. Qinxi silver ores occur in the rhyolitic ignimbrite of the Nanyuan Formation. In total, 400 tons of silver have been identified. The silver ore-bearing alteration veins are controlled by WNW–NW trending faults. For example, nine structural alteration zones with WNW–NW orientations were found at the edge of the Shimoshan basin (Figure 2).

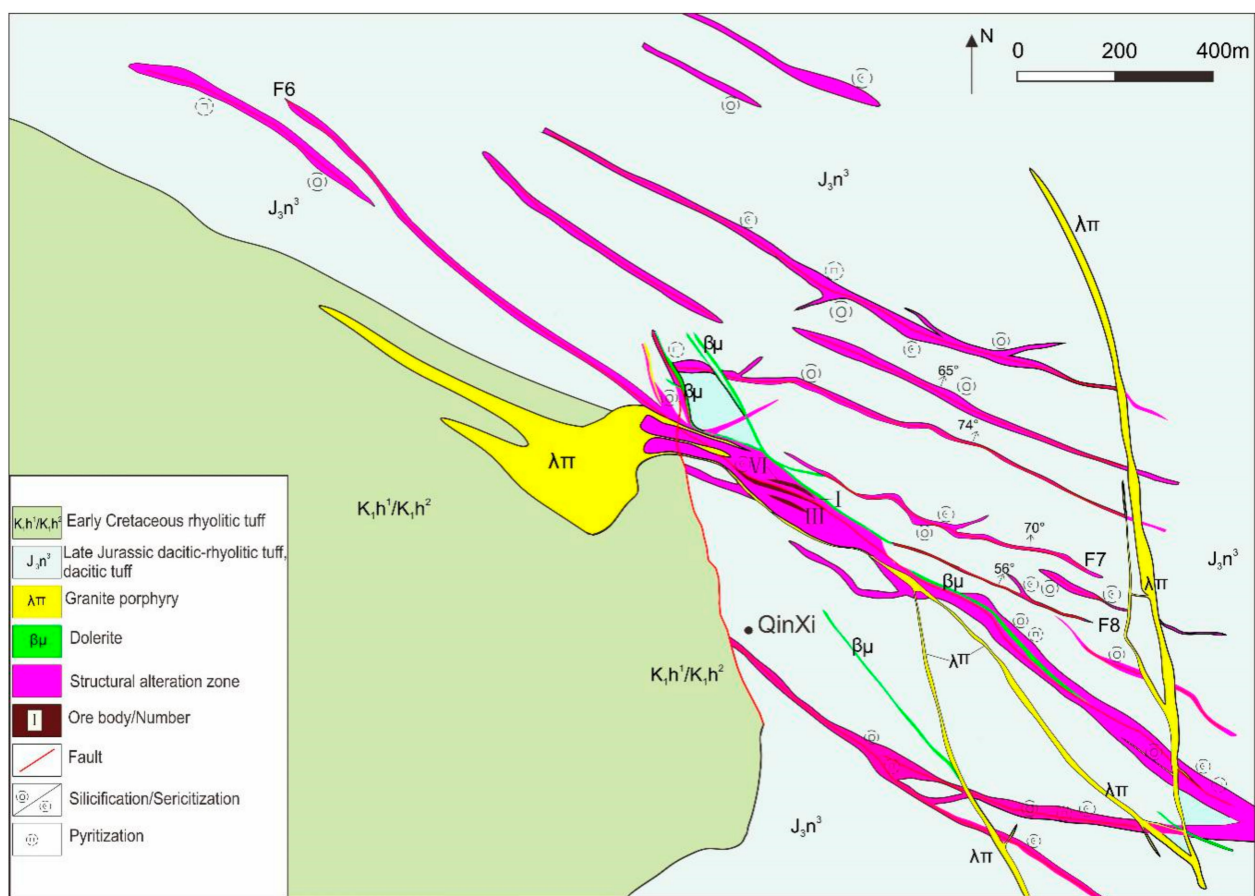


Figure 2. Geological map of the Qinxi deposit.

About 35 silver polymetallic ore bodies have been identified in the north–west trending mineralized belt. The gold and silver mineralization occurs over an outcrop area of about 1.6 km². Ore bodies are mainly distributed in the F6, F7, and F8 belts (Figure 2) and are generally uplifted to the northeast with representations of large and small ore veins. The morphology of the ore body is controlled mainly by the two northwesterly trending rhyolitic porphyry veins. The dip angles of the ore body vary from 45° to 80° and are concentrated at 60°–70°. The total size of the ore body is 400 m long and 100–150 m wide, with a controlled elevation from around 850 to 1130 m. Most of the ore bodies are concealed (Figure 3). Ores in Qinxi have typically crystallographic, metasomatic, and metamorphic textures and cataclastic, vein-like, reticular, massive, and brecciform structures (Figure 4). The ore minerals are mainly sphalerite, galena, and pyrite, followed

by chalcopyrite, argentite, silver-bearing chalcocite, bornite. Gangue minerals include quartz, sericite, kaolin, chlorite, pyrophyllite, and other medium to low temperature hydrothermal minerals.

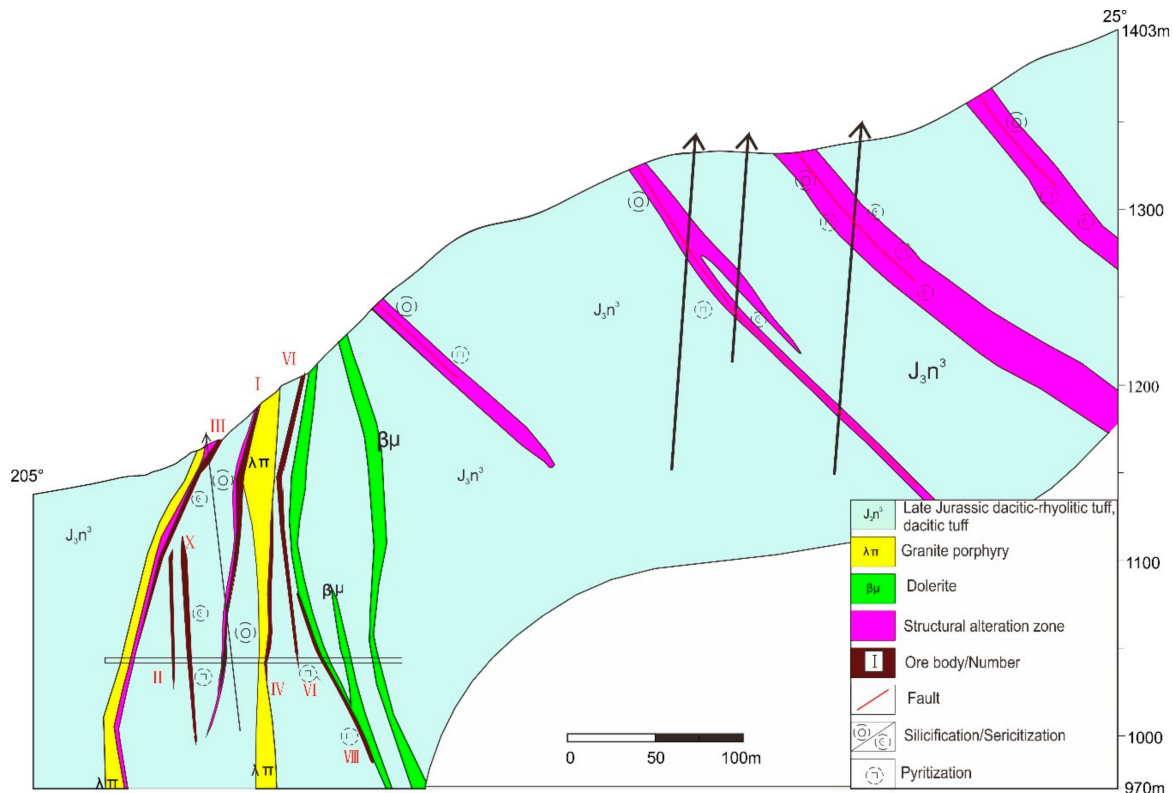


Figure 3. Number 3 section map in the mining area of the Qinxi deposit.

The wall rocks experienced medium to low temperature hydrothermal alterations along the fractures. The types of alteration include silicification, sericitization, manganese mineralization, kaolinization, carbonatization, chloritization, pyritization, lead–zinc mineralization, iron manganese mineralization, and limonitization (Figure 5). Silicification manifested as quartz veinlets and reticulated veins filled along the rock fractures (Figure 5a,b). Disseminated pyrite appears mainly in the ignimbrite and the contact interfaces of different types of rocks. Chlorites are dark-green in color and distributed in a planar manner (Figure 5c). Pyrophyllites are milky white or greenish gray and distributed on the fracture surface of the porphyry rhyolite (Figure 5a,c,d). Epidotes are light green and distributed along the rock fissures and mostly appear with chlorites (Figure 5c,f). The alteration types related to mineralization mainly include silicification, pyritization, and chloritization.

Wall rock alterations indicate the zoned spatial distribution from the center to the border: strong silicification → pyritization and/or lead–zinc mineralization → beresitization → rhodochrosite mineralization, pyrophyllitization, carbonatization, kaolinization, and chloritization. Vertical alterations are less obvious. The upper altered part features kaolinization, ferritization, and silicification with large and small quartz veins (“silica cap”) on the surface. The lower part is dominated by lead–zinc mineralization and chloritization.

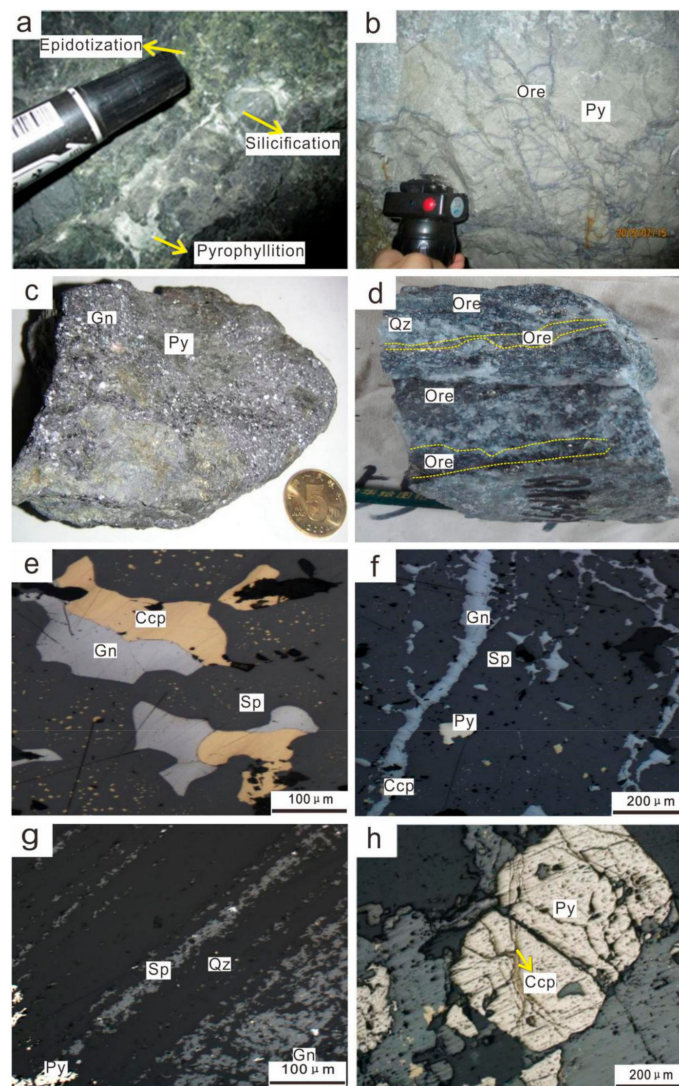


Figure 4. Typical structures of the ores. (a) Reticular vein-like ore and crystal caves; (b) breccia structure and lead–zinc veins; (c) massive lead, zinc, and silver ores; (d) vein-like lead, zinc, and silver ores; (e) crystal structure between sphalerite, galena, and chalcopyrite; (f) metasomatism structure (galena interspersed sphalerite in the form of veins and dykes); (g) metamorphic structure (directional deformation of pyrite and sphalerite due to a dynamic effect); and (h) mesh-vein structure. Sp—sphalerite, Gn—galena, Py—pyrite, Qz—quartz, Ccp—chalcopyrite.

The alteration features suggest that Qinxī ore is a typical epithermal silver deposit and is likely formed in an intermediate to acidic environment [30]. The main metallogenic stage belongs to the magmatic hydrothermal period and can be divided into four stages (Table 1) due to the character of the ore and the mineral compositions: (1) the phase of pyrite and quartz (stage I): Metal minerals in this stage comprise largely pyrite, with a small amount of sphalerite, galena, and magnetite. This is the early stage before significant silver mineralization happened; (2) the sulfide rich phase (stage II): In this stage, large numbers of metal sulfides, such as pyrite, galena, sphalerite, and chalcopyrite, appeared and are represented as different types of veins. These sulfides are distributed in tectonic fracture zones; (3) the silver sulfide mineral phase (stage III): Large numbers of silver bearing minerals like pyrite, sphalerite, galena, and chalcopyrite were formed in this stage by replacing early stage sulphides. These minerals are represented as fine veins and distributed in the rock fractures; (4) the quartz–carbonate phase (stage IV): This is the last

stage of hydrothermal alterations. Quartz and carbonate are the main formed minerals due to their lower fluid temperature.

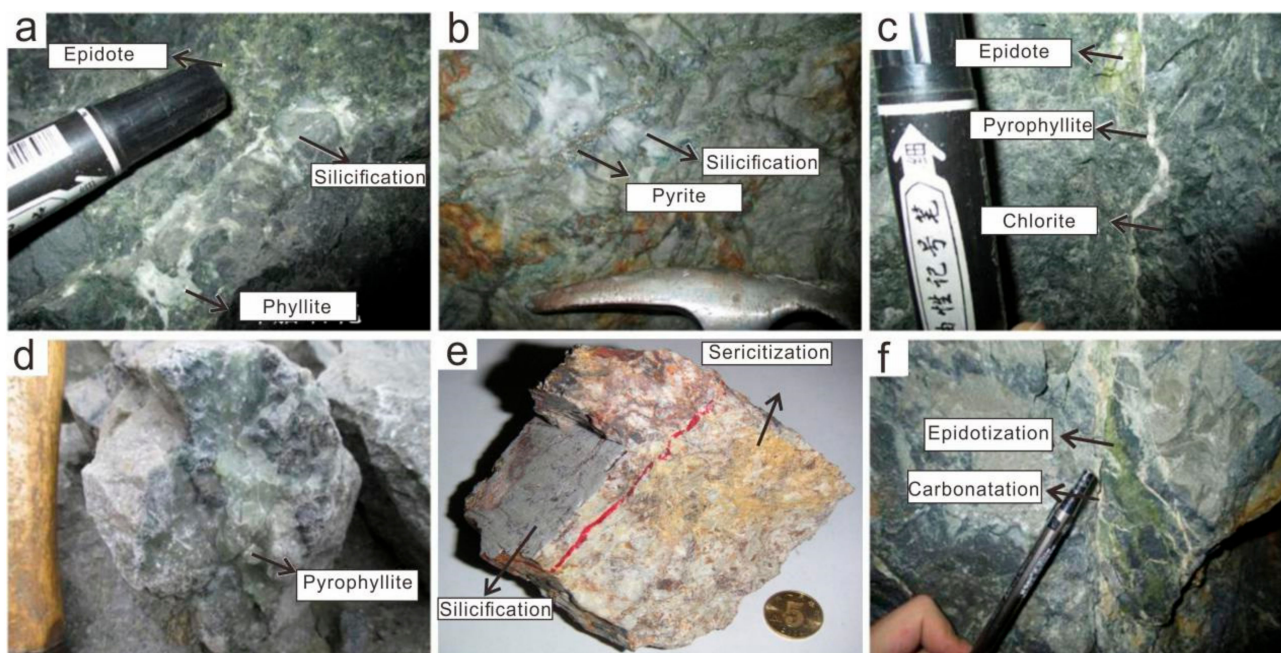


Figure 5. Typical alteration of rocks from the Qinxi deposit. (a) Vein-like silicification and small clumps of massive phyllite; (b) pyrite veins and small clumpy silicification; (c) epidote, pyrophyllite and chlorite in fissures; (d) massive pyrophyllite; (e) silicification and sericitization in altered veins; and (f) epidotization coexisting with carbonatation.

Table 1. Mineral formation sequence in the Qinxi Mine.

| Metallogenic Stage | I | II | III | IV |
|--------------------|---|----|-----|----|
| Hematite | █ | | | |
| Sericite | █ | █ | | |
| Pyrite | █ | █ | █ | █ |
| Chalcopyrite | | █ | █ | |
| Quartz | █ | █ | █ | █ |
| Sphalerite | | █ | █ | |
| Galena | | █ | █ | |
| Argentite | | | █ | █ |
| Crimson silver | | | █ | █ |
| Calcite | | | | █ |
| Fluorite | | | | █ |

4. Sample Collection and Analytical Methods

4.1. H–O–S–Pb Isotope Analysis

The H, O, S, Pb isotope samples were collected from #VII, #VI-7, #955, #985, and #1030 ore bodies. Sphalerite, galena, pyrite, chalcopyrite, and quartz, which have obviously associated relationships, were sampled in this study. All samples were fresh and manually crushed in an agate mortar, followed by sieving with to 40–60 meshes and cleaning and drying repeatedly. Lastly, we carefully selected the minerals under a microscope to ensure that each mineral had >99% purity.

- (1) H–O isotope analysis: H isotope samples were burst in carbon-containing glass ceramic tubes, thereby releasing the H₂O₂. The H₂O₂ reacted with carbon at high temperatures to generate H₂. H₂ was then carried via high purity helium flow into the

mass spectrometer MAT-253. The results were measured using V-SMOW. The analysis precision was better than 1‰, and the reference standards were Beida standard water (V-SMOW = −64.8‰) and Lanzhou standard water (V-SMOW = −84.55‰). The O isotope testing instrument was a MAT-253 gas isotope mass spectrometer. The measurement results were recorded as $\delta^{18}\text{O}$ with SMOW as the standard, and the analytical accuracy was better than $\pm 0.2\%$. The reference standards were GBW-04409 and GBW-04410 quartz standards. The hydrogen and oxygen isotopic compositions were determined by the stable isotope lab of the Beijing Research Institute of Uranium Geology. For the specific analysis methods, see [31].

- (2) S isotope analysis: After grinding the single mineral sample into a powder, Cu_2O was used as an oxidant to react with the sulfide single mineral mixture to generate SO_2 and freeze it for collection. The sample was determined by a mat-251 mass spectrometer. The test results were expressed as the $\delta^{34}\text{S}$ value of V-CDT, with an accuracy of $\pm 0.2\%$. The detection method and basis used GB/T0184.14-1997 “Determination of sulfur isotopic composition in sulfide”. The analysis was performed by The Laboratory of Stable Isotopes, Beijing Research Institute of Uranium Geology.
- (3) Pb isotope analysis: Pb isotope analysis was carried out via MC-ICP-MS at The State Key Laboratory of Geological Processes and Mineral Resources, China University of Geosciences (Wuhan). According to the standard GB/T17672-1999, “method for the determination of lead, strontium and neodymium isotopes in rocks”, the analytical instrument was a Resonetics-S155 laser ablation system. After the single mineral sample was dissolved by mixed acid, Pb was purified by the resin exchange method. The analytical accuracy of 1 μg for $^{208}\text{Pb}/^{204}\text{Pb}$ was better than 0.005%, as illustrated in [31].

4.2. Rb–Sr Isotope Analysis

Six sphalerite and galena samples from the VI-7 and VII ore veins in the Qinxu deposit were analyzed for their Rb–Sr isotopic composition. We first cleaned dirt from the surfaces of the original ore samples (leaving small original rock samples for inspection) and crushed the mineral grains to 40–80 meshes. Then, we put the grains under a microscope to select sphalerite and galena (10 g each). The selected samples were washed with diluted hydrochloric acid and ultra-pure water in an ultrasonic cleaning dish and then dried for later use.

We then added an $^{85}\text{Sr} + ^{84}\text{Sr}$ mixed diluent with about 1 g of the sample and dissolved the sample with the proper amount of chloroazotic acid. Rb and Sr were separated and purified by the cation resin exchange method, and the ratios of the Rb and Sr isotopes were analyzed using a thermal ionization mass spectrometer TRITON. The concentrations of Rb and Sr and the Sr isotope ratios in the samples were calculated by the isotope dilution method. For further detailed analysis procedures, please refer to [32]. In the whole process of isotope analysis, NBS987, NBS607, and GBW04411 standard materials were used to monitor the instruments and analysis process. The isotopic composition of $^{87}\text{Sr}/^{86}\text{Sr}$ of NBS987 was 0.71032 ± 0.00004 (2σ), which was consistent with the reference value of 0.71024 ± 0.00026 (2σ), within the margin of error. Rb, Sr, and ^{87}Sr of NBS607 were 523.60×10^{-6} , 65.54×10^{-6} , 1.20050 ± 0.00004 (2σ), which were consistent with the reference values ($523.90 \times 10^{-6} \pm 1.01 \times 10^{-6}$, $65.485 \times 10^{-6} \pm 0.30 \times 10^{-6}$, 1.20039 ± 0.00020 (2σ)). The ratios of Rb, Sr, and $^{87}\text{Sr}/^{86}\text{Sr}$ in GBW04411 were 249.90×10^{-6} , 158.80×10^{-6} , 0.76009 ± 0.00003 (2σ), which were consistent with the reference values ($249.47 \times 10^{-6} \pm 1.04 \times 10^{-6}$, $158.92 \times 10^{-6} \pm 0.70 \times 10^{-6}$, 0.75999 ± 0.00003 (2σ)). The whole process of isotope analysis sample preparation was completed in the super purification laboratory, and the background counts of Rb and Sr were 2×10^{-10} and 5×10^{-10} , respectively. Rb and Sr isotopes of sphalerite and galena in the main metallogenic period were determined by the solution method. The test work was completed by the modern analysis test center of Nanjing University. ISOPLLOT software [33] was used to determine the isochron age, and the decay constant value was $1.42 \times 10^{10} \text{ a}^{-1}$. A 2% error was used

for the ratio of the $^{87}\text{Sr}/^{86}\text{Sr}$ and 0.02% error for the value of $^{87}\text{Sr}/^{86}\text{Sr}$ in the isochron regression calculation.

5. Results

5.1. H and O Isotopes

The hydrogen and oxygen isotopic composition (including former data from [7,34]) are listed in Table 2 and illustrated in Figure 6. The $\delta\text{D}_{\text{V-SMOW}}$ values of quartz varied from -73.6‰ to 60.7‰ , with $\delta^{18}\text{O}_{\text{V-SMOW}}$ values from 4.1‰ to 6.0‰ . The uniform temperature averages for the ore-forming fluid inclusions in the quartz were determined to be 325 °C (I stage), 330 °C (II stage), 290 °C (III stage), and 273 °C (IV stage). The average values of the homogenization temperatures in each sample were used in the homogenization temperature calculation. Fluid inclusion temperatures in the quartz were analyzed at The China University of Geosciences (Wuhan) using a Linkam THMSC type with 600 stages. The test method used was the frozen homogenization method. The $\delta^{18}\text{O}_{\text{H}_2\text{O}}$ values of the quartz equilibrium fluid ranged from -2.5‰ to -0.1‰ and exhibited a progressive decrease from stage I to stage IV, according to the oxygen isotope fractionation equilibrium equation of the low temperature quartz–water system proposed in [35].

Table 2. Hydrogen and oxygen isotope composition of quartz in different stages in the Qinxi mining area (‰).

| Stage | Label | Mineral | Uniform Temperature | $\delta^{18}\text{O}_{\text{V-SMOW}}$ | $\delta\text{D}_{\text{V-SMOW}}$ | $\delta^{18}\text{O}_{\text{H}_2\text{O}}$ | Source |
|-----------|----------|----------------|---------------------|---------------------------------------|----------------------------------|--|--------------|
| Stage I | Q-6 | SiO_2 | 325 | 6 | -69 | -0.1 | This Article |
| Stage II | Q-25 | SiO_2 | 330 | 5.8 | -66.6 | -0.1 | This Article |
| | Q-26 | SiO_2 | 330 | 4.1 | -60.7 | -1.8 | This Article |
| Stage III | Q-8 | SiO_2 | 290 | 5.3 | -67.7 | -2.0 | This Article |
| Stage IV | Q-3 | SiO_2 | 273 | 5.4 | -73.6 | -2.5 | This Article |
| Unknown | DZ-1 | SiO_2 | 230 | | -49.3 | -5.04 | [34] |
| Unknown | DZ-2 | SiO_2 | 238 | | -87.5 | -8.51 | [34] |
| Unknown | ZK1 hole | SiO_2 | 235 | | -65.5 | -3.92 | [7] |

Citations: Oxygen isotope calculation formula: $\delta^{18}\text{O}_{\text{H}_2\text{O}} = \delta^{18}\text{O}_{\text{V-SMOW}} - 3.38 \times 10^6 T^{-2} + 3.40$ [35]. When calculating, T is the average temperature of the uniform temperature of the quartz fluid inclusion in the mineralization stage of the sample.

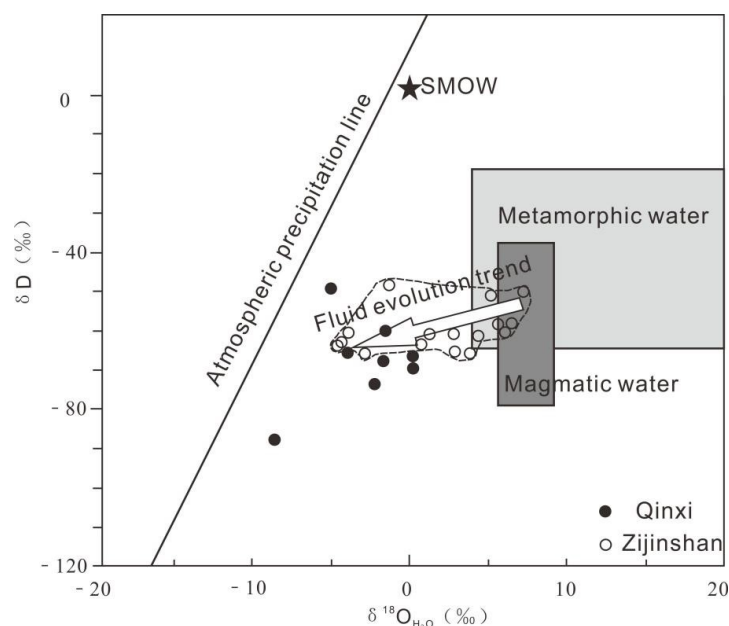


Figure 6. δD versus $\delta^{18}\text{O}_{\text{H}_2\text{O}}$ diagram from (Zijinshan data from [8,36]).

5.2. S Isotope Composition

The sulfur isotopic compositions are listed in Table 3. In total, 25 sulfides from the Qinxi ore deposit have a $\delta^{34}\text{S}$ range from -1.7‰ to 7.1‰ , with an average value of 0.92‰

and clustered around -1.7‰ ~ 4.1‰ . The $\delta^{34}\text{S}$ values of pyrite range from -1.3‰ to 7.1‰ , with an average of 1.30‰ ; the $\delta^{34}\text{S}$ values of sphalerite range from -1.7‰ to 0.8‰ , with an average of -0.43‰ ; the $\delta^{34}\text{S}$ values of galena range from -0.8‰ to 2.1‰ , with an average of 0.78‰ ; and the $\delta^{34}\text{S}$ values of chalcopyrite range from -1.7‰ to 0.8‰ , with an average of -0.43‰ . The sulfur isotopes from ore sulfide vary within a narrow range and are concentrated with a peak value of about 0.5‰ (Figure 7).

Table 3. Sulfur isotopic composition of the main sulfides in the Qinxi mining area (source from this article).

| Sample Serial Number | Stage | Mineral | $\delta^{34}\text{S}$ (‰) |
|----------------------|-----------|--------------------|---------------------------|
| TZ-6-2 | Stage I | FeS ₂ | 0.8 |
| TZL-6-3 | Stage I | FeS ₂ | 1.3 |
| TZS-1-2-5 | Stage I | FeS ₂ | 0.3 |
| TZL-4-1-1 | Stage I | FeS ₂ | 0.7 |
| TZL-4-1-2 | Stage I | FeS ₂ | 0.1 |
| TZ-11-1-9 | Stage II | FeS ₂ | -0.6 |
| TZ-25-1-9 | Stage II | FeS ₂ | -0.2 |
| G-28-2-2 | Stage II | FeS ₂ | 7.1 |
| G-28-4-3 | Stage II | FeS ₂ | 4.1 |
| TZW-2-1-7 | Stage II | FeS ₂ | 1.7 |
| TZW-2-3-6 | Stage II | FeS ₂ | 3.6 |
| TZ-11-1-8 | Stage II | ZnS | -1.5 |
| TZ-25-1-10 | Stage II | ZnS | -0.6 |
| G-28-2-3 | Stage II | ZnS | 0.8 |
| TZW-2-1-9 | Stage II | ZnS | 0.2 |
| TZ-2-2-6 | Stage II | ZnS | 0.2 |
| TZW-2-1-8 | Stage II | PbS | 0 |
| G-28-4-1 | Stage II | PbS | 2.1 |
| TZW-2-3-7 | Stage II | PbS | 1.7 |
| G-28-4-2 | Stage II | CuFeS ₂ | 4.1 |
| TZ-0-1-1 | Stage III | FeS ₂ | -0.2 |
| TZ-0-4-3 | Stage III | FeS ₂ | -1.3 |
| TZ-0-1-3 | Stage III | ZnS | -1.7 |
| TZ-0-4-2 | Stage III | PbS | -0.8 |
| TZ-0-1-2 | Stage III | CuFeS ₂ | 1.3 |

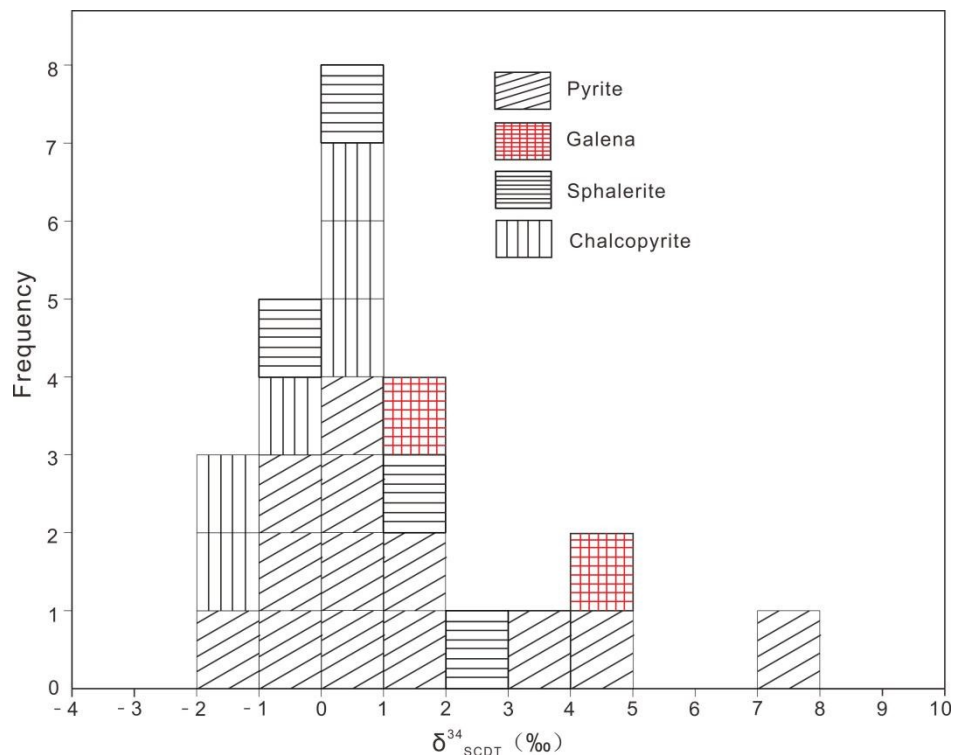


Figure 7. Frequency histogram of the S isotope composition of sulfide from the Qinxi deposit (data from Table 3).

5.3. Pb Isotopic Composition

The results of the lead isotope composition analysis for the sulfide minerals and magmatic rocks in the Qinxi silver polymetallic mining area are listed in Table 4. The content of radiogenic Pb in the sulfide minerals is extremely low. We corrected the Pb isotope composition of the whole rock using the methods in [37]. The range of $^{206}\text{Pb}/^{204}\text{Pb}$ values for the five galena samples varied from 18.447 to 18.513, with an average value of 18.478. The range of $^{207}\text{Pb}/^{204}\text{Pb}$ values varied from 15.623 to 15.703, with an average value of 15.660. The range of $^{208}\text{Pb}/^{204}\text{Pb}$ values varies from 38.673 to 38.947, with an average value of 38.811. The $^{206}\text{Pb}/^{204}\text{Pb}$ values from the six pyrite samples ranged from 18.406 to 18.562, with an average value of 18.507. The pyrites had $^{207}\text{Pb}/^{204}\text{Pb}$ values from 15.580 to 15.766, with an average value of 15.682, and $^{208}\text{Pb}/^{204}\text{Pb}$ values from 38.740 to 39.163, with an average value of 38.903. After age correction, the range of $^{206}\text{Pb}/^{204}\text{Pb}$ from the three whole rock samples ranged from 18.421 to 18.605, with an average value of 18.532; the $^{207}\text{Pb}/^{204}\text{Pb}$ values ranged from 15.590 to 15.772, with an average value of 15.688; and the $^{208}\text{Pb}/^{204}\text{Pb}$ values ranged from 38.591 to 39.183, with an average value of 38.934. The above analytical values show that the Pb isotope variation ranges of ore in the Qinxi deposit are quite small.

Table 4. Analysis results of the Pb isotope of ore sulfide and the lead isotope of rock in Qinxi mining area.

| Sample Serial Number | Lithology | Mineral | Measurement Result | | | μ | $\Delta\beta$ | $\Delta\gamma$ | Source |
|----------------------|-------------------|------------------|-----------------------------------|-----------------------------------|-----------------------------------|-------|---------------|----------------|--------------|
| | | | $^{208}\text{Pb}/^{204}\text{Pb}$ | $^{207}\text{Pb}/^{204}\text{Pb}$ | $^{206}\text{Pb}/^{204}\text{Pb}$ | | | | |
| QXK-7 | Pb–Zn–Ag Ore | PbS | 38.947 | 15.703 | 18.513 | 9.66 | 24.74 | 46.44 | This Article |
| QXK-23 | Pb–Zn–Ag Ore | PbS | 38.920 | 15.695 | 18.509 | 9.64 | 24.21 | 45.71 | This Article |
| Unknown | Ag–Pb–Zn Ore | PbS | 38.673 | 15.623 | 18.447 | 9.51 | 19.55 | 39.43 | [34] |
| Unknown | Pb–Zn–Ag Ore | PbS | 38.743 | 15.637 | 18.454 | 9.53 | 20.52 | 41.85 | [34] |
| Unknown | Ag–Pb–Zn Ore | PbS | 38.774 | 15.641 | 18.467 | 9.54 | 20.76 | 42.49 | [7] |
| QXK-1 | Ag–Pb–Zn Ore | FeS ₂ | 39.163 | 15.766 | 18.562 | 9.77 | 28.85 | 52.24 | This Article |
| QXK-11 | Pb–Zn–Ag Ore | FeS ₂ | 39.072 | 15.733 | 18.553 | 9.71 | 26.69 | 49.80 | This Article |
| QXK-26 | Pb–Zn–Ag Ore | FeS ₂ | 39.039 | 15.726 | 18.551 | 9.70 | 26.24 | 48.91 | This Article |
| Unknown | Rhyolite porphyry | FeS ₂ | 38.740 | 15.630 | 18.495 | 9.51 | 19.97 | 40.88 | [34] |
| Unknown | Rhyolite porphyry | FeS ₂ | 38.794 | 15.654 | 18.473 | 9.56 | 21.66 | 43.54 | [34] |
| Unknown | Ag–Pb–Zn Ore | FeS ₂ | 38.608 | 15.580 | 18.406 | 9.42 | 16.64 | 36.63 | [34] |
| QXL-6 | Rhyolite porphyry | Whole rock | 39.029 | 15.703 | 18.605 | 9.65 | 24.74 | 48.64 | This Article |
| QXW-2 | Fused tuff | Whole rock | 39.183 | 15.772 | 18.569 | 9.79 | 29.24 | 52.78 | This Article |
| Unknown | Altered tuff | Whole rock | 38.591 | 15.590 | 18.421 | 9.44 | 17.3 | 36.24 | [7] |

Citations: In this paper, the pb isotopic composition data of the whole rock was corrected according to the age of the volcanic rocks in the Nanyuan Formation ($t = 140.1$ Ma, $\text{Th}/\text{U} = 1.03$, [24]). Using the Greokit software package to calculate the source region characteristic parameters, $\mu = ^{238}\text{U}/^{204}\text{Pb}$, $\Delta\beta = [(^{207}\text{Pb}/^{204}\text{Pb})_d(t)/(^{207}\text{Pb}/^{204}\text{Pb})_m(t) - 1] \times 10^3$, $\Delta\gamma = [(^{208}\text{Pb}/^{204}\text{Pb})_d(t)/(^{208}\text{Pb}/^{204}\text{Pb})_m(t) - 1] \times 10^3$, and d and m, respectively, represent the ore Pb and mantle Pb at time t in the metallogenic era [38]; reference calculation for the mantle Pb isotopic composition [34]: mantle growth formula, $\mu = 7.8$, $^{232}\text{Th}/^{238}\text{U} = 4.04$, and $t_0 = 4.57$ Ga; original Pb composition: $(^{206}\text{Pb}/^{204}\text{Pb})_0 = 9.307$, $(^{207}\text{Pb}/^{204}\text{Pb})_0 = 10.294$, $(^{208}\text{Pb}/^{204}\text{Pb})_0 = 29.476$.

5.4. Rb–Sr Geochronology

The Rb and Sr concentrations and isotopic compositions of the six samples from Qinxi are shown in Table 5. The isochronous lines were constructed from different mineral combinations between single minerals and paragenetic minerals so that the isochronous ages of single minerals and symbiotic minerals could be constrained to each other, thus improving the accuracy of the isochron lines and obtaining relatively accurate metallogenic ages [39]. The Rb–Sr isochronic line obtained in our study shows a good linear relationship (Figure 8). The ISOPLOT package software was used to calculate the isochron ages. Mineral galena and sphalerite had an Rb–Sr isochron age of 130 ± 2.0 Ma (Figure 8a), with an initial $I_{Sr} = 0.71033$ and MSWD = 1.7. The single mineral galenas had an Rb–Sr isochronal age of 130 ± 7.1 Ma (Figure 8b), with $I_{Sr} = 0.71032$ and MSWD = 2.0, indicating the same isochron age for both galena and sphalerite within the margin of error.

Table 5. Rb–Sr composition of sphalerite and galena in the Qinxi deposit.

| Sample | Mineral | Rb (10^{-6}) | Sr (10^{-6}) | $^{87}\text{Rb}/^{86}\text{Sr}$ | $^{87}\text{Sr}/^{86}\text{Sr}$ | $^{87}\text{Sr}/^{86}\text{Sr} \pm 1\sigma$ |
|--------|---------|------------------|------------------|---------------------------------|---------------------------------|---|
| QXK-5 | Sp | 0.9048 | 0.8854 | 3.015 | 0.715974 | 0.71597 ± 0.00003 |
| QXK-7 | Sp | 0.8732 | 0.6061 | 4.256 | 0.718143 | 0.71814 ± 0.00005 |
| QXK-1 | Gn | 0.2841 | 4.557 | 0.1846 | 0.710738 | 0.71074 ± 0.00002 |
| QXK-19 | Gn | 0.1639 | 1.528 | 0.3159 | 0.710847 | 0.71084 ± 0.00003 |
| QXK-22 | Gn | 0.3743 | 0.7325 | 1.507 | 0.713131 | 0.71313 ± 0.00004 |
| QXK-23 | Gn | 0.4127 | 1.476 | 0.8242 | 0.711805 | 0.71181 ± 0.00006 |

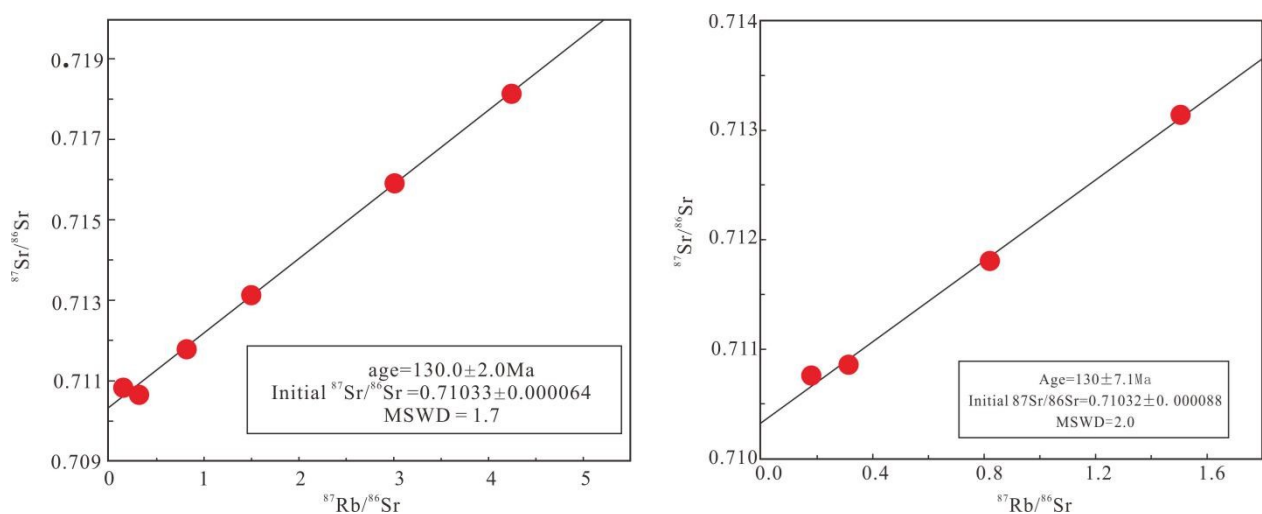


Figure 8. Rb–Sr Isochronal dating diagrams: (a) data from paragenetic minerals l assemblages and (b) data from single galena.

6. Discussion

6.1. Ore Forming Age

The samples analyzed in this study were all large Pb–Zn samples from the main metallogenic stages at different locations of the Qinxi ores with high purity. No gangue minerals or fractures were observed under the microscope [40]. Our dating results suggest the Qinxi silver ore was formed at 130 ± 2 Ma (MSWD = 1.70) (Figure 8a). The sphalerite and galena with different Rb and Sr concentrations had similar $^{87}\text{Sr}/^{86}\text{Sr}$ values (Table 5). No linear correlations were observed in the $1/\text{Rb}$ vs. $^{87}\text{Rb}/^{86}\text{Sr}$ and $1/\text{Sr}$ vs. $^{87}\text{Sr}/^{86}\text{Sr}$ diagrams (Figure 9). Thus, the initial ratios of $^{87}\text{Sr}/^{86}\text{Sr}$ in the sphalerite and galena were well-preserved.

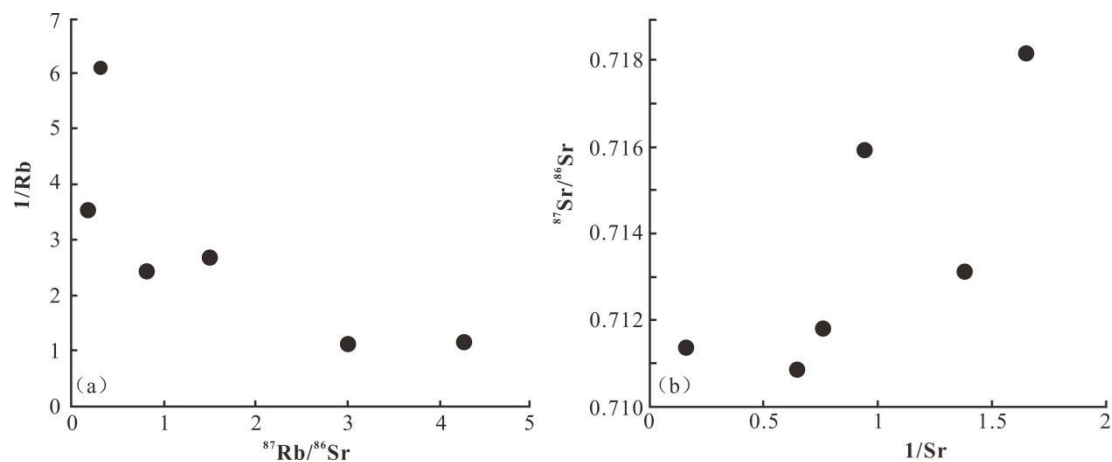


Figure 9. $1/Rb$ versus $^{87}Rb/^{86}Sr$ and $^{87}Sr/^{86}Sr$ versus $1/Sr$ diagrams from sphalerite and accompanying galena in the Qinxi deposit.

Some geochronology data from typical volcanic hydrothermal polymetallic deposits in the southeast coastal area have been reported, such as the Zhilingtou gold and silver deposits (127 to 165 Ma; the Rb–Sr isochronal age of fluid inclusion in quartz [41]), the Zijinshan gold–copper deposits (122.2 ± 3.9 Ma; Rb–Sr isochronal age of fluid inclusion in quartz [42]), the Bitian silver deposit (94.7 ± 2.3 Ma; ^{40}Ar – ^{39}Ar age from valencianite [43]), the Haoshi silver deposit (104 Ma, Rb–Sr isochronal age of fluid inclusion in quartz [40]), and the Xiaban gold deposits (125 Ma; Rb–Sr isochronal age from sericite, [44]). Most of the above deposits have metallogenic ages from the early Cretaceous to the late Cretaceous. Our dating results also fall into this period, which belongs to the early Cretaceous, within the period of Yanshanian Pacific plate subduction and large-scale lithospheric thinning tectonic events in eastern China [44].

6.2. Sources of the Metallogenic Material

H and O isotopes are effective tracers for ore-forming fluid sources [45,46]. Our results are relatively concentrated between the magma water and meteoric precipitation in the δD – $\delta^{18}O_{H_2O}$ diagram (Figure 6) ($\delta D = -85\text{‰} \sim -40\text{‰}$, $\delta^{18}O_{H_2O} = 5\text{‰} \sim 9.5\text{‰}$) [47] and show a trend of deviation from the magmatic water to the direction of meteoric precipitation, indicating that the ore-forming fluid in the study area represents the mixing of magmatic (volcanic) gas–liquid and shallow groundwater. For comparison, the data from adjacent and contemporaneous Zijinshan ore deposits are also plotted in Figure 6. The H and O isotopic compositions of Zijinshan ore have wider ranges and are closer to the magmatic water box, while those of the Qinxi deposit are closer to the atmospheric precipitation area, suggesting different proportions of the two reservoirs. Some samples from Zijinshan ore were plotted away from the magmatic water area, which may have been influenced by the early fluid evolution from magmatic water to atmospheric precipitation in the later stage [46,48]. Recent studies have shown that meteoric water plays an important role in the hydrothermal system [49], and increasingly more evidence suggests that middle and low temperature hydrothermal fluids are mainly the mixed genesis of primary magmatic water and meteoric precipitation. The H and O isotopic compositions of the Qinxi deposit are consistent with the composition of many medium to low temperature hydrothermal deposits with ore-forming fluids mainly from the mixed water of volcanic hydrothermal and meteoric precipitation.

The sulfide in Qinxi ore is mainly pyrite without sulfate minerals. Under low oxygen fugacity, the sulfur in the ore-forming fluid exists in its HS^- , S^{2-} form [36]. The $\delta^{34}S$ value in the pyrite is similar to that of the ore-forming fluid, which approximately represents the total sulfur isotopic composition of the hydrothermal fluid [1]. Sulfides in Qinxi ore (Pyrite $\delta^{34}S = -1.3\text{‰} \sim 7.1\text{‰}$, avg. = 1.34‰ ; Galena $\delta^{34}S = -0.8\text{‰} \sim 2.1\text{‰}$, avg. = 0.75‰ ; Sphalerite $\delta^{34}S = -1.7\text{‰}$ to 0.8‰ , avg. = -0.43‰) have $\delta^{34}S$ values ranging from -1.7‰ to

7.1‰, mainly concentrated around -2‰ to 2‰ , with an average value of 0.92‰ (Table 3, Figure 7), which is similar to the value of the original mantle sulfur (-3‰ ~ 3‰). The sulfide $\delta^{34}\text{S}$ values (galenite > sphalerite > pyrite) indicate that the sulfur isotope fractionation in the metallogenic hydrothermal system of Qinxi ore has reached its equilibrium.

Qinxi silver ore was formed in Nanyuan sedimentary–volcanic rocks, which developed a fracture system. Hence, the S isotope of the sulfide could be easily changed via contamination from atmospheric precipitation. We speculate that the initial sulfide in Qinxi had a mantle-value isotopic composition, but contamination from the subsequent addition of atmospheric precipitation led to a wide range of sulfide $\delta^{34}\text{S}$ values. The sulfide S isotope in Zijinshan ore presents $\delta^{34}\text{S}$ values mainly from -5‰ to 1‰ , but most also fall into the primitive mantle sulfur (-3‰ ~ 3‰) range [8]. Thus, the sulfur in both the Zijinshan and Qinxi deposits is likely from magma or extracted from the volcanic rocks.

Lead isotopes can also provide a source of information for ore deposits [50]. Because metal sulfide usually contains extremely low concentrations of U and Th, the sulfide's Pb isotope compositions should be directly inherited from the mineralization fluid [40]. The sulfide lead isotopes from the Qinxi deposit are relatively concentrated, indicating a homogeneous metallogenic source. In Figure 10a, all samples are plotted near the evolutionary line of the upper crust and orogenic belt, suggesting that the Pb in sulfide mainly came from the upper crust. In addition, the Pb isotope ratio of the Qinxi ore was similar to that of the Zijinshan ore where we found in the adjacent region (Figure 8a), suggesting that these two deposits may have similar Pb sources.

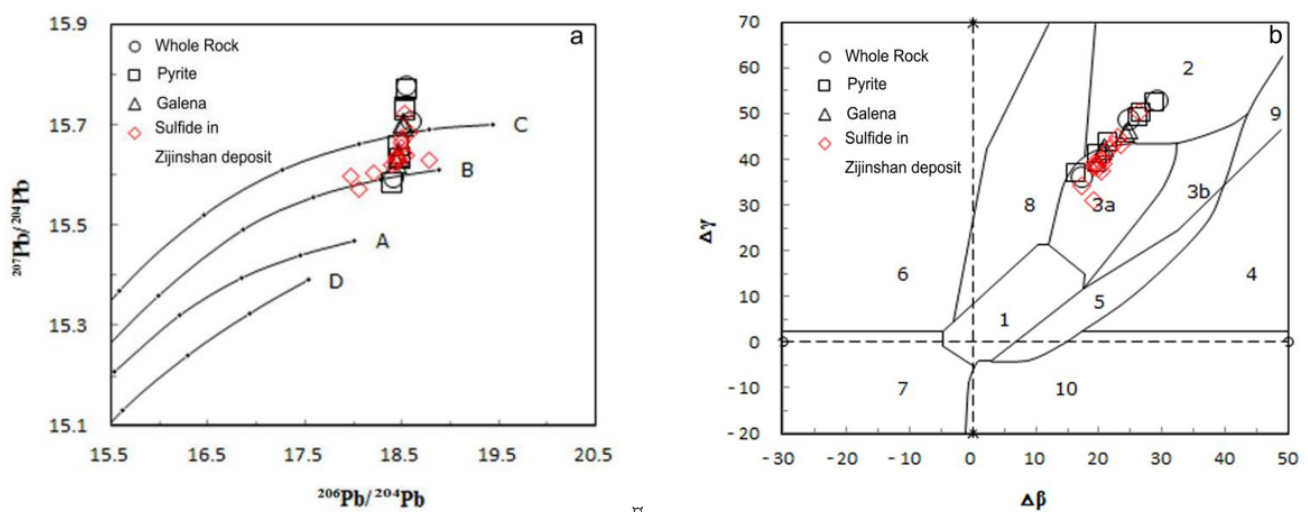


Figure 10. (a) Lead isotope discriminate diagram from [2]. (b) Lead $\Delta\gamma$ versus $\Delta\beta$ diagram from [50]. A—Mantle; B—Orogene; C—Upper crust; D—Lower crust. 1—Mantle origin lead; 2—Crustal origin lead; 3—Mixed lead from upper crust and mantle at the subducted zone. 3a—Magmatism; 3b—Sedimentation; 4—Chemically deposited lead; 5—Lead from undersea hot water; 6—Lead from the medium to deep metamorphism; 7—Lead in the lower crust of the deep metamorphism; 8—Lead in the orogenic belts; 9—Lead in the ancient shale from the upper crust; 10—Lead from retrometamorphism.

Crustal-derived Pb is characterized by a high μ value [50]. The average μ value of sulfide in the Qinxi deposit is 9.60 (>9.58), which is within the values of a crustal source. Zhu proposed using a genetic classification diagram to trace the source region of Pb. The Geokit software [51] was used to calculate the relevant parameters of the Pb isotope according to the single-stage Pb evolution model, and the results are shown in Table 3. Most of our samples fall into the upper crustal Pb area. Some Pb isotopic data fall into the subduction zone Pb range (Figure 8b). This result is consistent with the distribution features of the Pb isotope data in the Pb tectonic model map of Zartman and Doe, as discussed above.

The typical sulfide and whole rock lead isotopes in the Qinxi and Zijinshan deposit [8] are similar to those of the early Cretaceous intrusive volcanic rocks in the adjacent area. Li [52] modeled binary mixing using Pb content and the Pb isotope from the Badu group metamorphic rocks and Mesozoic volcanic rocks as end-members, and the results showed that 71~92 wt.% Pb in the ore was from volcanic rock, with only 8~29 wt.% from the metamorphic rocks. Thus, a genetic relationship between Mesozoic volcanic eruptions and Qinxi mineralization should be present. Combined with the crustal-derived Sr ($^{87}\text{Sr}/^{86}\text{Sr}$)_i = 0.7103) isotopes, we suggest that the mineralization materials are mainly from the crust.

6.3. Genesis of Qinxi Silver Ore

The Qinxi deposit is located in the east part of the South China plate and belongs to the southeastern margin of the Eurasian continental plate. It lies in the Meso–Cenozoic giant tectonic–magmatic belt of the Pacific Rim [53,54], which features large volumes of volcanic rocks. The southeast coastal area of China experienced a transformation from the Tethys tectonic domain to the Pacific tectonic domain. During this period, Mesozoic orogeny was formed. According to metallogenic characteristics and continental dynamic background, orogeny can be divided into early, middle and late stages, accompanied by three large stages of mineralization. The first stage was characterized by mantle magma upwelling and generated a certain number of mafic rocks between 185 to 170 Ma [22,55]. It reflects the local “extensional cracking” of lithosphere and the upwelling of mantle material. The second stage generated a large amount of S-type granotoids and W, Sn, Pb, and Zn ores within the ages of 185–170 Ma, likely under an extensional geological background. The last stage extended from 140 to 65 Ma. Lithospheric thinning and crustal extension were the dominant geological process during this stage [20,56].

Our studies demonstrated that the Qinxi deposit was formed at ca. 130 Ma, which coincides with the period of lithospheric thinning and crustal extension in the region. According to En-gebretson [57], the Izanagi plate was subducted to Eurasia from the middle Jurassic (180 Ma) to the late Jurassic (about 145 Ma) in the northwest direction. This subduction caused asthenospheric upwelling and underplating along the northeast trending fault and melted the crust at different locations. At the same time, the subduction angle gradually increased due to gravity and wall rock resistance, which migrated the magmatism to the eastern ocean direction. This hypothesis agrees with the fact that the Mesozoic volcanic rocks in the southeastern coast were distributed along the northeast trending fault and migrated from west to east. The “X” shape fractures featuring brecciated ore structures developed in the Qinxi area. These structures were mostly generated in an extension environment [3]. At the same time, the prosperous magma–hydrothermal system generated by Cretaceous volcanic magma activity was helpful for the formation of silver ore [58].

As discussed above, the H–O–S–Pb isotopes suggest that the ore-forming materials were mainly from the crust. The widespread lower temperature minerals, such as low-Fe-content (FeS 1.35 wt.% [34]) light color sphalerite, were possibly formed by low-temperature magmatic–hydrothermal activities. The distribution of phyllite and carbonate in the region reveals the gradual evolution of ore-forming fluid from an early acid to later intermediate composition [59,60]. The geological and geochemical characteristics of the Qinxi deposit are similar to those of typical middle-low temperature hydrothermal deposits, such as the Zijinshan deposit in Fujian Province and the Jinguashi deposit in Taiwan Province [61,62]. Therefore, we suggest that mineralization of the silver deposits occurred at a shallow depth and was related to deep intermediate-acid magmatic hydrothermal mineralization fluid.

In recent years, concealed porphyry copper deposits have been found below the epithermal polymetallic deposits in the Zijinshan ore field, and the similar metallogenic ages indicate a uniform porphyry system [63,64], which is similar to those that occurred in North and South America and the Philippines [65,66]. In these systems, the magmatic water contributed to both the porphyry and epithermal mineralization, and the epithermal fluids

contained more meteoric components [67,68]. The late epithermal fluids could dissolve significant amounts of gold and silver from porphyry Cu–Au deposits and therefore advantage the formation of distal epithermal Au–Ag deposits [69]. From the perspective of porphyry systems, we deduced that the Qinxi silver deposit is a distal epithermal deposit of a porphyry system, and deep concealed Cu–Mo–Au ore deposits exist at the contact zone between the Qinxi ore and the deep-seated intermediate-felsic pluton.

7. Conclusions

- (1) Rb–Sr isochronal dating precisely revealed that the Qinxi silver deposit was formed ca. 130 Ma, confirming an early Cretaceous silver mineralization event in South China.
- (2) The symbiotic minerals and ore assemblages suggest that Qinxi ore is a typical middle to low temperature hydrothermal deposit.
- (3) Systematic studies of H, O, S, and Pb isotopes in the sulfide indicate that the ore-forming materials in the Qinxi silver deposit are mainly of crustal origin. The ore-forming fluid is a mixture of magmatic water and meteoric water.
- (4) Both geological features and isotopic compositions suggest that the Qinxi silver deposit has similar ore-forming sources with the adjacent Zijinshan deposit and that there may be concealed Cu–Mo–Au ore below the Qinxi silver deposit.

Author Contributions: Conceived and designed the experiments: S.Z., W.L. Performed the experiments: S.Z., W.L. Analyzed the data: S.Z., W.L. Contributed reagents/materials/analysis tools: S.Z., W.L., J.Z.; Contributed to the writing of the manuscript: S.Z., W.L., J.Z. and Q.G. All authors have read and agreed to the published version of the manuscript.

Funding: This work was supported by The Fujian Geological Exploration Bureau project “Study on Metallogenic Conditions and Prospecting Targets of Ag–Au(Cu) Polymetallic Deposit in Qinxi Mining Area, Zhouning County, Fujian Province” (No: FGEB[2016]76) is funded.

Institutional Review Board Statement: Not applicable.

Informed Consent Statement: Not applicable.

Conflicts of Interest: The authors declare no conflict of interest.

References

1. Chen, Y.H.; Wang, D.H. Four Main Topics Concerning the Metallogeny Related to Mesozoic Magmatism in South China. *Geotecton. Metallog.* **2012**, *363*, 315–321.
2. Zhu, X.D.; Liu, Z.P.; Wu, J.Z. Diagram showing the characteristics of lead isotopes from the silver ore-deposits of the volcanic terrain in the coastal area of Fujian and Zhejiang provinces. *Geol. Fujian* **1996**, *4*, 177–189.
3. Wu, G.G.; Zhang, D.; Peng, R.M.; Wu, J.S.; Gao, T.J.; Chen, B.L.; Wang, Q.F.; Di, Y.J.; Zhang, X.X. Study on The Evolution Regularity of Mineralization Ages in Southeastern China. *Earth Sci. Front.* **2004**, *1*, 237–247.
4. Gao, Y.; Zhang, Z.J.; Xiong, Y.H.; Zuo, R.G. Mapping mineral prospectivity for Cu polymetallic mineralization in southwest Fujian Province, China. *Ore Geol. Rev.* **2016**, *75*, 16–28. [[CrossRef](#)]
5. Shi, H.H. Analysis of Metallogenic Geological Condition and Potential of Deposits in Daan of Fujian. Ph.D. Thesis, China University of Geosciences, Beijing, China, 2008; p. 67.
6. Zhao, F.F.; Liu, X.F.; Zhu, L.M.; Chu, Y.T.; Chun, H.L.; Cai, Y.W. Geochemistry trace of metallization for polymetal field in Yangjiaba, Lueyang, Shanxi Province. *Acta Petrol. Sin.* **2010**, *26*, 1465–1478.
7. Jiang, Y.H.; Chen, H.N.; Wu, Q.H.; Chen, S.Z. Geological Characteristics, Genesis and Further Prospecting Direction of Ag–Pb–Zn Mineralization of Qinxi-Guansi, Zhouning, Fujian. *Geol. Explor.* **1994**, *4*, 21–25.
8. Liang, Q.L.; Jiang, S.H.; Bai, D.M.; Wang, S.H. Sources of ore-forming materials of epithermal deposits in Zijinshan orefield in Fujian Province: Evidence from H, O, S and Pb isotopes. *Miner. Depos.* **2015**, *3*, 533–546.
9. Li, Q.; Santosh, M.; Li, S.-R.; Zhang, J.-Q. Petrology, geochemistry and zircon U–Pb and Lu–Hf isotopes of the Cretaceous dykes in the central North China Craton: Implications for magma genesis and gold metallogeny. *Ore Geol. Rev.* **2015**, *67*, 57–77. [[CrossRef](#)]
10. Lin, J.D. Metallogenetic Characteristics of Bijianshan–Qinxi Ag, Polymetal Ore Belt, Fujian Province. *Contrib. Geol. Miner. Resour. Res.* **2003**, *18*, 132–136.
11. Zhong, S.F. Geological Features and Deep Prospecting of Qinxi Silver Polymetallic Deposit in Zhongning County, Fujian Province. *Geol. Fujian* **2016**, *2*, 122–131.
12. Wang, D.Z.; Shen, W.Z. Genesis of granitoids and crustal evolution in southeast China. *Earth Sci. Front.* **2003**, *3*, 209–220.
13. Li, X. Subdivision and characteristic of tectonic units in Fujian Province. *Glob. Geol.* **2013**, *32*, 549–557.

14. Li, S.-N.; Ni, P.; Bao, T.; Xiang, H.-L.; Chi, Z.; Wang, G.-G.; Huang, B.; Ding, J.-Y.; Dai, B.-Z. Genesis of the Ancun epithermal gold deposit, southeast China: Evidence from fluid inclusion and stable isotope data. *J. Geochem. Explor.* **2018**, *195*, 157–177. [[CrossRef](#)]
15. Ma, Y.; Jiang, S.-Y.; Chen, R.-S.; Li, X.-X.; Zhu, L.; Xiong, S.-F. Hydrothermal evolution and ore genesis of the Zhaiping Ag–Pb–Zn deposit in Fujian Province of Southeast China: Evidence from stable isotopes (H, O, C, S) and fluid inclusions. *Ore Geol. Rev.* **2019**, *104*, 246–265. [[CrossRef](#)]
16. Lin, K.; Zhang, Y.H.; Wang, Y.J. Lithospheric thinning in the North China Block: A numerical approach on thermal perturbation and tectonic extension. *Geotecton. Metallog.* **2004**, *28*, 8–14.
17. Zhong, J.; Chen, Y.J.; Qi, J.P.; Chen, J.; Dai, M.C.; Li, J. Geology, fluid inclusion and stable isotope study of the Yueyang Ag–Au–Cu deposit, Zijinshan orefield, Fujian Province, China. *Ore Geol. Rev.* **2017**, *86*, 254–270. [[CrossRef](#)]
18. Li, S.-N.; Ni, P.; Bao, T.; Li, C.-Z.; Xiang, H.-L.; Wang, G.-G.; Huang, B.; Chi, Z.; Dai, B.-Z.; Ding, J.-Y. Geology, fluid inclusion, and stable isotope systematics of the Dongyang epithermal gold deposit, Fujian Province, southeast China: Implications for ore genesis and mineral exploration. *J. Geochem. Explor.* **2018**, *195*, 16–30. [[CrossRef](#)]
19. Li, B.; Jiang, S.-Y. Genesis of the giant Zijinshan epithermal Cu–Au and Luoboling porphyry Cu–Mo deposits in the Zijinshan ore district, Fujian Province, SE China: A multi-isotope and trace element investigation. *Ore Geol. Rev.* **2017**, *88*, 753–767. [[CrossRef](#)]
20. Hua, R.M.; Chen, P.R.; Zhang, W.L.; Lu, J.J. Three major metallogenic events in Mesozoic in South China. *Miner. Depos.* **2005**, *24*, 99–107.
21. Zhang, G.; Guo, A.; Wang, Y.; Li, S.; Dong, Y.; Liu, S.; He, D.; Cheng, S.; Lu, R.; Yao, A. Tectonics of South China continent and its implications. *Sci. China Earth Sci.* **2013**, *56*, 1804–1828. [[CrossRef](#)]
22. Ni, P.; Wang, G.-G.; Cai, Y.-T.; Zhu, X.-T.; Yuan, H.-X.; Huang, B.; Ding, J.-Y.; Chen, H. Genesis of the Late Jurassic Shizitou Mo deposit, South China: Evidences from fluid inclusion, H O isotope and Re Os geochronology. *Ore Geol. Rev.* **2017**, *81*, 871–883. [[CrossRef](#)]
23. Li, L.; Li, S.-R.; Santosh, M.; Li, Q.; Gu, Y.; Lü, W.-J.; Zhang, H.-F.; Shen, J.-F.; Zhao, G.-C. Dyke swarms and their role in the genesis of world-class gold deposits: Insights from the Jiaodong peninsula, China. *J. Asian Earth Sci.* **2016**, *130*, 2–22. [[CrossRef](#)]
24. Duan, Z.; Xing, G.F.; Yu, M.G.; Zhao, X.L.; Jin, G.D.; Chen, Z.H. Time Sequence and Geological Process of Late Mesozoic Volcanic Activities in the Area of Zhejiang-Fujian Boundary. *Geol. Rev.* **2013**, *59*, 454–468.
25. Guo, F.; Fan, W.; Li, C.; Zhao, L.; Li, H.; Yang, J. Multi-stage crust–mantle interaction in SE China: Temporal, thermal and compositional constraints from the Mesozoic felsic volcanic rocks in eastern Guangdong–Fujian provinces. *Lithos* **2012**, *150*, 62–84. [[CrossRef](#)]
26. Hu, X.; Gong, Y.; Pi, D.; Zhang, Z.; Zeng, G.; Xiong, S.; Yao, S. Jurassic magmatism related Pb–Zn–W–Mo polymetallic mineralization in the central Nanling Range, South China: Geochronologic, geochemical, and isotopic evidence from the Huangshaping deposit. *Ore Geol. Rev.* **2017**, *91*, 877–895. [[CrossRef](#)]
27. Yuan, L.; Chi, G.; Wang, M.; Li, Z.; Xu, D.; Deng, T.; Geng, J.; Hu, M.; Zhang, L. Characteristics of REEs and trace elements in scheelite from the Zhuxi W deposit, South China: Implications for the ore-forming conditions and processes. *Ore Geol. Rev.* **2019**, *109*, 585–597. [[CrossRef](#)]
28. Chen, T.S. On the geologic characteristics and prospecting directions of Tianchi silver polymetallic ore in Shouning County, Fujian Province. *Geol. Fujian* **2017**, *104*, 228–236. (In Chinese)
29. Lu, L.; Liang, T.; Zhao, Z.; Liu, S. A Unique association of scheelite and magnetite in the Tiemuli W–Fe skarn deposit: Implications for Early Cretaceous metallogenesis in the Nanling Region, South China. *Ore Geol. Rev.* **2018**, *94*, 136–154. [[CrossRef](#)]
30. Li, S.T.; Zhu, X.Y.; Wang, J.B. Review of studies on terrestrial sub-volcanic deposits. *Miner. Depos.* **2014**, *51*, 705–706.
31. Voudouris, P.; Melfos, V.; Spry, P.G.; Bonsall, T.A.; Tarkian, M.; Solomos, C. Carbonate-replacement Pb–Zn–Ag±Au mineralization in the Kamariza area, Lavrion, Greece: Mineralogy and thermochemical conditions of formation. *Miner. Pet.* **2008**, *94*, 85–106. [[CrossRef](#)]
32. Li, W.B.; Huang, Z.L.; Xu, D.R. Rb–Sr isotopic method on Pb–Zn ore deposits: A review. *Geotecton. Metall.* **2002**, *4*, 436–441.
33. Pieter, V. IsoplotR: A free and open toolbox for geochronology. *Geosci. Front.* **2018**, *9*, 1479–1493.
34. Dai, Q.Z. Ore-forming Process of the Qinxi Silver-lead-zinc Deposit in Zhounin County and Its Ore-finding Target. *Geol. Fujian* **2008**, *2*, 175–185.
35. Clayton, R.N.; O’Neil, J.R.; Mayeda, T.K. Oxygen isotope exchange between quartz and water. *J. Geophys. Res. Space Phys.* **1972**, *77*, 3057–3067. [[CrossRef](#)]
36. So, C.-S.; Dequan, Z.; Yun, S.-T.; Daxing, L. Alteration-mineralization zoning and fluid inclusions of the high sulfidation epithermal Cu–Au mineralization at Zijinshan, Fujian Province, China. *Econ. Geol.* **1998**, *93*, 961–980. [[CrossRef](#)]
37. Xing, G.F.; Yang, Z.L.; Xue, H.M.; Shen, J.L.; Zhao, Y.; Mao, J.R.; Tao, K.Y. The Study Progress and Orientation of Mesozoic Volcanic Rock belts in Southeast Continent, China. *Geol. Jiangsu* **1999**, *23*, 221–224.
38. Zhu, B.Q. *The Theory and Application of Isotope System in Earth Science Also on the Evolution of Crust and Mantle in Chinese Mainland*; Science Press: Beijing, China, 1998; pp. 216–230.
39. Zheng, W.; Chen, M.H.; Xu, L.G.; Zhao, H.J.; Ling, S.B.; Wu, Y.; Hu, Y.G.; Tian, Y.; Wu, X.D. Rb–Sr isochron age of Tiantang Cu–Pb–Zn polymetallic deposit in Guangdong Province and its geological significance. *Miner. Depos.* **2013**, *32*, 259–272.
40. Li, C.Y.; Liu, T.G.; Ye, L. Large and ultra-large silver deposits related to volcanic rocks in China. *Sci. China Ser. D* **2002**, *32*, 69–77.
41. Chen, H.S. Research on the Isotope for Zijinshan Ore Deposit. *Geotecton. Metallog.* **1996**, *4*, 348–360.

42. Chen, Y.C.; Wang, D.H.; Xu, Z.G.; Huang, F. Outline of Regional Metallogeny of Ore Deposits Associated with the Mesozoic Magmatism in South China. *Geotecton. Metallog.* **2014**, *2*, 219–229.
43. Zhang, D.Q.; Shen, H.Q.; Li, D.X.; Feng, C.Y. The Porphyry-Epithermal Metallogenic System in the Zijinshan Region, Fujian Province. *Acta Geol. Sin.* **2003**, *77*, 253–261.
44. Chen, R.S.; Lin, D.Y.; Jiang, J.L. Dynamical Mechanism and Tectonics Significance of Early Jurassic Volcanism in Fujian Province. *Geol. Fujian* **2007**, *27*, 156–165.
45. Hoefs, J. *Stable Isotope Geochemistry*, 2nd ed.; Springer: Berlin/Heidelberg, Germany; New York, NY, USA, 1980.
46. Jiang, S.-H.; Liang, Q.-L.; Bagas, L.; Wang, S.-H.; Nie, F.-J.; Liu, Y.-F. Geodynamic setting of the Zijinshan porphyry–epithermal Cu–Au–Mo–Ag ore system, SW Fujian Province, China: Constrains from the geochronology and geochemistry of the igneous rocks. *Ore Geol. Rev.* **2013**, *53*, 287–305. [[CrossRef](#)]
47. Faure, G. *Principles of Isotope Geology*, 2nd ed.; John Wiley & Sons: New York, NY, USA, 1986; pp. 183–199.
48. Chen, J.; Chen, Y.J.; Zhong, J.; Sun, Y.; Li, Z.; Qi, J.F. Fluid inclusion study of the Wuziqilong Cu deposit in the Zijinshan ore field, Fujian Province. *Acta Petrol. Sin.* **2011**, *5*, 1425–1438.
49. Miron, G.D.; Wagner, T.; Wälle, M.; Heinrich, C.A. Major and trace-element composition and pressure–temperature evolution of rock-buffered fluids in low-grade accretionary-wedge metasediments, Central Alps. *Contrib. Miner. Petrol.* **2012**, *165*, 981–1008. [[CrossRef](#)]
50. Zhu, Y.F.; An, F. Geochemistry of hydrothermal mineralization: Taking gold deposit as an example. *Earth Sci. Front.* **2010**, *2*, 42–52.
51. Lu, Y.F. GeoKit-A geochemical toolkit for Microsoft Excel. *Geochimica* **2004**, *33*, 459–464.
52. Wang, H.L.; Li, Y.J.; Xu, S.Q.; Jiang, Y.J.; Li, N.P.; Xiao, G.L.; Zhou, J.B. Latest advances of researches on epithermal gold deposits. *GOLD* **2009**, *7*, 9–13.
53. Zhao, X.; Yu, S.; Mao, J.; Liu, K.; Yu, M.; Jiang, Y.; Chen, Z.; Hou, K.; Peng, Y. Compression between microcontinents in the Cathaysian Block during the early Yanshanian: Petrogenesis of the Tangquan pluton in Southwest Fujian Province, Southeast China. *Geol. J.* **2016**, *52*, 970–991. [[CrossRef](#)]
54. Zhao, X.; Yu, S.; Jiang, Y.; Mao, J.; Yu, M.; Chen, Z.; Xing, G. Petrogenesis of two stages of Cretaceous granites in south-west Fujian Province: Implications for the tectonic transition of South-east China. *Geol. J.* **2018**, *54*, 221–244. [[CrossRef](#)]
55. Zhao, X.; Mao, J.; Liu, K.; Li, Z.; Ye, H.; Zhou, J.; Hu, Y. Petrogenesis of the Jurassic adakitic rocks in Gan-Hang Belt South China: Response to the Palaeo-Pacific Plate oblique subduction. *Geol. J.* **2017**, *53*, 2019–2044. [[CrossRef](#)]
56. Zhao, X.L.; Yu, S.Y.; Mao, J.R.; Liu, K.; Yu, M.G.; Jiang, Y.; Chen, Z.H.; Hou, K.J.; Peng, Y.B. A geochemical and geochronological study of the early Cretaceous, extension-related Honggong ferroan (A-type) granite in southwest Zhejiang Province, southeast China. *Geol. Mag.* **2018**, *55*, 549–567. [[CrossRef](#)]
57. Engebretson, D.C.; Cox, A.; Gordon, R.G. *Relative Motions Between Oceanic and Continental Plates in the Pacific Basin*; Geological Society of America: Boulder, CO, USA, 1985.
58. Soloviev, S.G. Geology, mineralization, and fluid inclusion characteristics of the Kumbel oxidized W-Cu-Mo skarn and Au-W stock work deposit, Tien-Shan, Kyrgyzstan. *Miner. Depos.* **2015**, *50*, 187–220. [[CrossRef](#)]
59. Mao, J.; Xie, G.Q.; Li, X.F.; Mei, Y.X. Mesozoic large scale mineralization and multiple lithospheric extension in south China. *Earth Sci. Front.* **2004**, *11*, 45–55.
60. Yu, B. *Study on Evolution of Mesozoic Magmatic Rocks and Metallogenic Feature of Zijinshan Orefield*; Chinese Academy of Geological Science: Beijing, China, 2012; pp. 1–30. (In Chinese)
61. Huang, R.S. Igneous Series and Epithermal Porphyry Cu–Au–Ag Mineralization System in the Zijingshan Ore Field, Fujian Province. *J. Geomech.* **2008**, *1*, 74–86.
62. Li, B.; Zhao, K.D.; Zhang, Q.; Xu, Y.M.; Zhu, Z.Y. Petrogenesis and geochemical characteristics of the Zijinshan granitic complex from Fujian Province, South China. *Acta Petrol. Sin.* **2015**, *31*, 811–828. (In Chinese)
63. Liang, Q.L.; Jiang, S.H.; Wang, S.H.; Li, C.; Zeng, F.G. Re-Os dating of molybdenite from the Luoboling porphyry Cu–Mo deposit in the Zijinshan ore field of Fujian Province and its geological significance. *Acta Geol. Sin.* **2012**, *86*, 1113–1118.
64. Pan, T.W.; Yuan, Y.; Lv, Y.; Shi, W.Q. The Early-Cretaceous tectonic evolution and the spatial-temporal framework of magmatism–mineralization in Zijinshan ore-field, Fujian Province. *J. Geomech.* **2019**, *25*, 61–75.
65. Waters, P.J.; Cooke, D.R.; Gonzales, R.I.; Phillips, D. Porphyry and Epithermal Deposits and ⁴⁰Ar/³⁹Ar Geochronology of the Baguio District, Philippines. *Econ. Geol.* **2011**, *106*, 1335–1363. [[CrossRef](#)]
66. Sillitoe, R.H. Porphyry Copper Systems. *Econ. Geol.* **2010**, *105*, 3–41. [[CrossRef](#)]
67. Cooke, D.R.; Deyell, C.L.; Waters, P.J.; Gonzales, R.I.; Zaw, K. Evidence for Magmatic-Hydrothermal Fluids and Ore-Forming Processes in Epithermal and Porphyry Deposits of the Baguio District, Philippines. *Econ. Geol.* **2011**, *106*, 1399–1424. [[CrossRef](#)]
68. Watanabe, Y.; Hedenquist, J.W. Mineralogic and stable isotope zonation at the surface over the El Salvador porphyry copper deposit, Chile. *Econ. Geol.* **2001**, *96*, 1775–1797. [[CrossRef](#)]
69. Cooke, D.R.; Simmons, S.G. Characteristics and genesis of epithermal gold deposits. *Rev. Econ. Geol.* **2000**, *13*, 221–244.